

## Short Communication

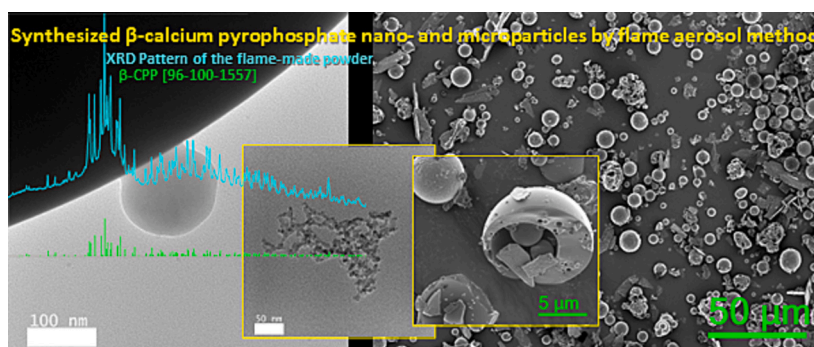
Fast-facile synthesis of single-phase nanocrystalline  $\beta$ - $\text{Ca}_2\text{P}_2\text{O}_7$  powder by an aerosol synthesis methodAlireza Charmforoushan<sup>\*</sup>, Miika Sorvali, Jyrki M. Mäkelä

Aerosol Physics Laboratory, Physics Unit, Faculty of Engineering and Natural Sciences, Tampere University, Tampere, Finland

## HIGHLIGHTS

- Continuous synthesis of  $\beta$ -calcium pyrophosphate ( $\beta$ -CPP) without post-heat treatment.
- Single-phase  $\beta$ -CPP powder was synthesized by a one-step flame aerosol method.
- Spherical  $\beta$ -CPP nanoparticles could be synthesized by applying liquid flame spray.
- Flame-made  $\beta$ -CPP particles have shown (nano)porous structure with high surface area.

## GRAPHICAL ABSTRACT



## ARTICLE INFO

## Keywords:

Nanocrystalline materials  
Porous materials  
Calcium pyrophosphate  
Nanostructure  
Liquid flame spray  
Continuous one-step synthesis

## ABSTRACT

Recently,  $\beta$ -phase of calcium pyrophosphate has gained wide attention for potential in different applications. In this communication, we report for the first time an ultra-fast, cost-effective, and facile one-step synthesis of single-phase  $\beta$ -CPP powder without post-heat treatment by applying liquid flame spray (LFS). LFS is a scalable, continuous, and adjustable one-step flame-based aerosol synthesis method. The effect of Ca/P ratio on structural properties was investigated.  $\beta$ - $\text{Ca}_2\text{P}_2\text{O}_7$  could be successfully synthesized in spherical nano- and micron-sized particles, as well as plate-like particles. The synthesized single-phase powder exhibited high thermal stability and relatively high specific surface area with different (nano)porous structures.

## 1. Introduction

Calcium phosphate-based materials (CP) have been widely applied in lots of different areas over the past few decades due to their specific properties. Mostly their orthophosphate forms (for instance, hydroxyapatite (HA), which constitutes the inorganic phase of human bone tissues) have been used in various biomedical applications. However,

calcium orthophosphates have not individually shown desired mechanical properties as well as bioresorbability and/or biodegradability, and thus they are frequently combined with other biomaterials/bioceramics, and/or phases such as calcium pyrophosphate ( $\text{Ca}_2\text{P}_2\text{O}_7$ , CPP) [1–4]. CPP has drawn increasing attention as a promising material for biomedical applications owing to its very good bioresorbability, solubility, osteoconductivity, mechanical properties, and biocompatibility

<sup>\*</sup> Corresponding author.

E-mail address: [alireza.charmforoushan@tuni.fi](mailto:alireza.charmforoushan@tuni.fi) (A. Charmforoushan).

<https://doi.org/10.1016/j.powtec.2023.119342>

Received 7 July 2023; Received in revised form 13 November 2023; Accepted 27 December 2023

Available online 3 January 2024

0032-5910/© 2024 The Authors. Published by Elsevier B.V. This is an open access article under the CC BY license (<http://creativecommons.org/licenses/by/4.0/>).

[5–8]. CPP has three polymorphs:  $\gamma$ -CPP,  $\beta$ -CPP, and high-temperature  $\alpha$ -CPP which is a metastable phase and can transform back to the  $\beta$ -polymorph by cooling [8,9]. Literature reports have indicated that the presence of  $\beta$ -CPP in some biomaterials/bioceramics can significantly increase their mechanical properties and biodegradability [10–12]. Moreover, Lee et al. [13] demonstrated that  $\beta$ -CPP implants are more appropriate for bone graft substitutes than HA implants, as  $\beta$ -CPP implants have shown much better osteoconductivity, bioresorbability, and biodegradability compared to HA implants.  $\beta$ -CPP shows also promise for other applications such as water purification [14], catalysis [15], and electrical systems [16,17]. Besides, as CPP has a very good modifiable matrix, it has been widely studied for photo-/thermoluminescent applications by introduction of different ions [18–22].

Since  $\beta$ -CPP is the most stable of the phases and has outstanding potential for applications and advantages compared with the others, developing a low-cost, facile, and large-scale (or fast and continuous) synthesis method for  $\beta$ -CPP especially with high purity and in nanosize/structure i.e., with a high surface area, offers an interesting research area. Therefore, other researchers have introduced novel wet-chemical synthesis methods for  $\beta$ -CPP that they claim to be simple, fast, and/or economical with the assistance of microwaves or the efficient use of waste materials as the precursors [2,14,17,22–24]. However, these are discontinuous, and can be considered relatively time-consuming, and complicated as they involve numerous steps. Moreover, to the best of our knowledge, these synthesis methods always require a sintering/calcination process at a high temperature to fabricate the  $\beta$ -phase.  $\beta$ -CPP can be also synthesized by thermal conversion of the low-temperature phase ( $\gamma$ -CPP) or brushite (dicalcium phosphate dihydrate), but the applied chemical synthesis methods for the other phases have similar disadvantages, and the transformation temperature to pure  $\beta$ -CPP is  $>800^\circ\text{C}$  [7,8,13]. It is a major challenge in the synthesis of calcium pyrophosphates as large pyrophosphate anions have low diffusion mobility; they need high temperature formation as well as a long duration of sintering/calcination. The concerning economic and environmental aspects related to energy consumption engendered the development of synthesis methods for these kinds of functional materials at lower temperatures [25–27].

So far, no synthesis method has been reported that does not need any post-heat treatment to form the  $\beta$ -CPP. We attempted to realize this via using liquid flame spray (LFS) synthesis method. LFS is an ultra-short synthesis time method that is scalable, reproducible, continuous, adjustable, and relatively low-cost [28–31]. LFS process is a flame-based aerosol synthesis method, able to generate single component micro-and/or nanoparticles. A solution consisting of precursor liquid in water/ethanol solution is sprayed into a turbulent, high temperature  $\text{H}_2/\text{O}_2$ -flame [32]. The precursor solution is atomized by one of the gas flows into droplets that go through liquid-to-solid reactions or evaporate, to be chemically converted and nucleated into micro-and/or nanoparticles. Eventually, an aerosol mixture of micron-and/or nano-sized particles is formed with a continuous throughput in the order of (milli)grams per minute (depends on nozzle size and feeding rate of the precursor solution) and can be collected as a powder after the flame.

The present communication deals with an ultra-fast, convenient, and continues one-step synthesis of nanocrystalline single-phase  $\beta$ - $\text{Ca}_2\text{P}_2\text{O}_7$  powder by LFS method without using any kind of post-heat treatment. Furthermore, the effect of precursors ratio on structural properties of the flame-made particles are investigated.

## 2. Materials and methods

Calcium nitrate tetrahydrate ( $\text{Ca}(\text{NO}_3)_2 \cdot 4\text{H}_2\text{O}$ , Merck) and ammonium phosphate dibasic ( $(\text{NH}_4)_2\text{HPO}_4$ , Sigma-Aldrich) were used as the precursors of Ca and P, respectively, with different molar ratios. The former one was dissolved in ethanol, and the latter one was dissolved in deionized water. After that, Ca and P solutions were mixed and stirred for 15 min, then the precursor solution was fed into a turbulent  $\text{H}_2/\text{O}_2$ -

flame with 2 ml/min feeding rate. Thereafter, generated aerosol particles were collected directly from the gas flow as a powder with an electrostatic precipitator described by Sorvali et al. [33–35]. The volume ratio of water to ethanol was adjusted 3/2, and total concentration of the precursors was fixed at 0.4 M for all samples. The  $\text{H}_2$  (combustion gas) and  $\text{O}_2$  (atomizer) gas flow rates were adjusted to 20 l/min and 10 l/min, respectively. Besides, a 5 l/min flow rate of  $\text{N}_2$  gas was added between them to push the flame further from the burner head. The gases were introduced through annular rings of a liquid flame spray burner which was earlier described and referred to as KP burner by Aromaa et al. [30].

The collected samples were named CPP-1.0, CPP-1.3, and CPP-1.5, as the molar ratio of Ca/P was adjusted to 1.0, 1.3, and 1.5, respectively. They were characterized by X-ray diffraction (XRD,  $\text{CuK}\alpha$  radiation,  $2\theta$  range of  $10$ – $80^\circ$  with step size of  $0.026^\circ$ ) using a Panalytical Empyrean multipurpose X-ray diffractometer (PANalytical B.V.). In addition, a field-emission scanning electron microscope (FE-SEM, Zeiss Crossbeam 540) with an energy-dispersive X-ray spectrometer (EDS, Oxford Instruments XMax<sup>N</sup> 80) and a high-resolution (scanning) transmission electron microscope (HR-(S)TEM, JEOL JEM-F200, operating at 200 kV) with a Jeol Dual EDS were used to characterize the samples.  $\text{N}_2$  adsorption-desorption isotherms of the samples were acquired by a Micropore Gas Adsorption Analyzer (Micromeritics 3Flex 3500, at  $-196^\circ\text{C}$ ). Besides, the specific surface area (SSA) was measured by the Brunauer–Emmett–Teller (BET) method using the data in the relative pressure range of 0.06–0.30. Moreover, the thermal decomposition behavior of the collected powders was evaluated with Simultaneous Thermal Analysis (STA (TGA (Thermogravimetric Analysis) – DSC (Differential Scanning Calorimetry)), Netzsch STA 449 F3 JUPITER) in the range of  $30$ – $1400^\circ\text{C}$  degree with a  $10^\circ\text{C}/\text{min}$  heating rate.

## 3. Results and discussion

The XRD patterns of the synthesized samples are presented in Fig. 1. The CPP-1.0 XRD pattern peaks accurately match only the reference XRD data of  $\beta$ -CPP (96–100-1557), so it can be assessed that single-phase  $\beta$ -CPP has been successfully synthesized. In addition, as can be revealed by comparison of the CPP-1.0 and CPP-1.3 patterns in Fig. 1a, the positions of the pattern peaks of the samples correspond to each other. There are two weak background humps in the XRD pattern of all samples, the first one at  $\sim 30^\circ$  and the latter one at  $\sim 45^\circ$  that indicate amorphous calcium phosphate (ACP,  $\text{Ca}_x\text{H}_y(\text{PO}_4)_z \cdot n\text{H}_2\text{O}$ ,  $3 \leq n \leq 4.5$ ,  $1.2 \leq \text{Ca/P ratio} \leq 2.2$ ) [36,37]. However, these background humps can also be a result of overlapping peaks that are wide due to nanoscale crystallites. The mean crystallite sizes of the CPP-1.0 and CPP-1.3 were calculated as 46.3 and 39.5 nm, respectively, by size-strain plot (SSP) method [25]. As the XRD pattern of the samples has many overlapped peaks at high angles, the SSP method should be the most accurate method over other methods such as Williamson–Hall (W–H) [38,39]. However, the mean crystallite size of the samples was also calculated by W–H as 49.5 and 46.9 nm for CPP-1.0 and CPP-1.3, respectively, which supports the SSP results.

As can be seen in Fig. 1a, the intensity counts of the mentioned background humps have risen with an increasing ratio of Ca/P from 1.0 (CPP-1.0) to 1.3 (CPP-1.3). Therefore, there could be some amorphous particles in CPP-1.3. Hence, raising the ratio of Ca/P from 1.0 can cause the ACP to form as its Ca/P ratio is  $>1.2$ . Raising the Ca/P ratio to 1.5 changed the XRD pattern completely, and many other phases appeared, such as brushite ( $\text{CaHPO}_4 \cdot 2\text{H}_2\text{O}$ , 96–900-7309), monetite ( $\text{CaHPO}_4$ , 96–210-6185), tricalcium phosphate (TCP,  $\text{Ca}_3\text{P}_2\text{O}_8$ , 96–900-5866), and HA ( $\text{Ca}_5\text{O}_{13}\text{P}_3$ , 96–901-4314), as can be revealed in Fig. 1b for CPP-1.5. It is worth mentioning that, by heating the sample at  $200^\circ\text{C}$  (H-CPP-1.5) some of brushite peaks disappeared and the intensity of some others obviously decreased which are indicated by blue solid-and dashed-line arrows, respectively, in Fig. 1b. Thus, brushite phase evaporated and/or transformed into another phase, which is in good

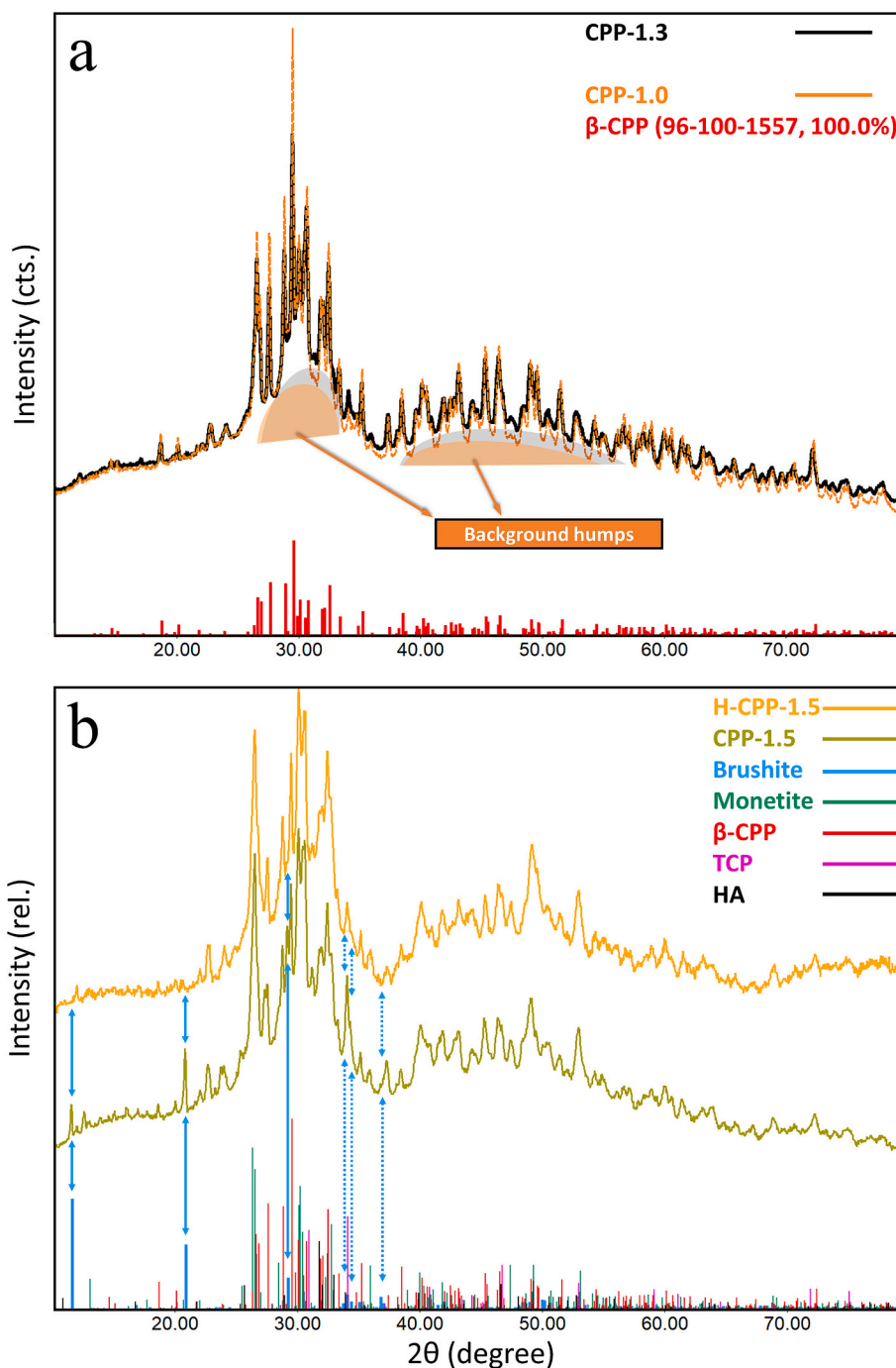


Fig. 1. XRD patterns of the synthesized samples.

agreement with the STA analysis of CPP-1.5. TGA curve of CPP-1.5 has  $-1.3\%$  weight loss before  $200\text{ }^{\circ}\text{C}$ , where a weak endothermic effect appeared in its DSC curve, as shown in the inset panel in Fig. 2. Therefore, structural water in brushite evaporated before  $200\text{ }^{\circ}\text{C}$ , and a phase transformation occurred, as was revealed by the XRD analysis. Besides, additional higher weight losses ( $-9.08\%$  and then  $-3.22\%$ ) are caused by increasing the temperature to around  $500$  and then  $715\text{ }^{\circ}\text{C}$ , which correspond with exothermic and endothermic effects in DSC analysis, respectively. These can be due to phase formations of  $\gamma$ -CPP and then  $\beta$ -CPP at  $500$  and  $715\text{ }^{\circ}\text{C}$ , respectively, that are in good agreement with literature [7,8]. Likewise, the weight losses are illustrated in the TGA curve of CPP-1.3, but they are weaker than for the CPP-1.5 one, so the amount of ACP in CPP-1.3 powder should not be

very high. On the other hand, there are not any sharp weight losses in the mentioned areas for CPP-1. The total weight loss is around  $-2\%$ , as can be seen in Fig. 2. This indicates a good thermal stability for the flame-made  $\beta$ -CPP powder. There is a sharp endothermic effect in DCS curves ( $\sim 1300\text{ }^{\circ}\text{C}$ ) after a strong descent that started gradually around  $800\text{ }^{\circ}\text{C}$ . Therefore, the phase transformation from  $\beta$  to  $\alpha$  could occur around  $1300\text{ }^{\circ}\text{C}$  similar to results of other researchers [18,40].

The  $\text{N}_2$  adsorption-desorption isotherms of the samples are shown in Fig. 3a. According to the IUPAC classification [41], there is a type  $\text{H}_3$  hysteresis loop without any limiting adsorption at high  $P/P_0$  in the isotherms of the CPP-1.3 and CPP-1.5, while the loop is much smaller for the CPP-1. The mentioned hysteresis loop illustrates aggregated plate-like particles possessing slit-shaped pores. The SSA of CPP-1.3 and

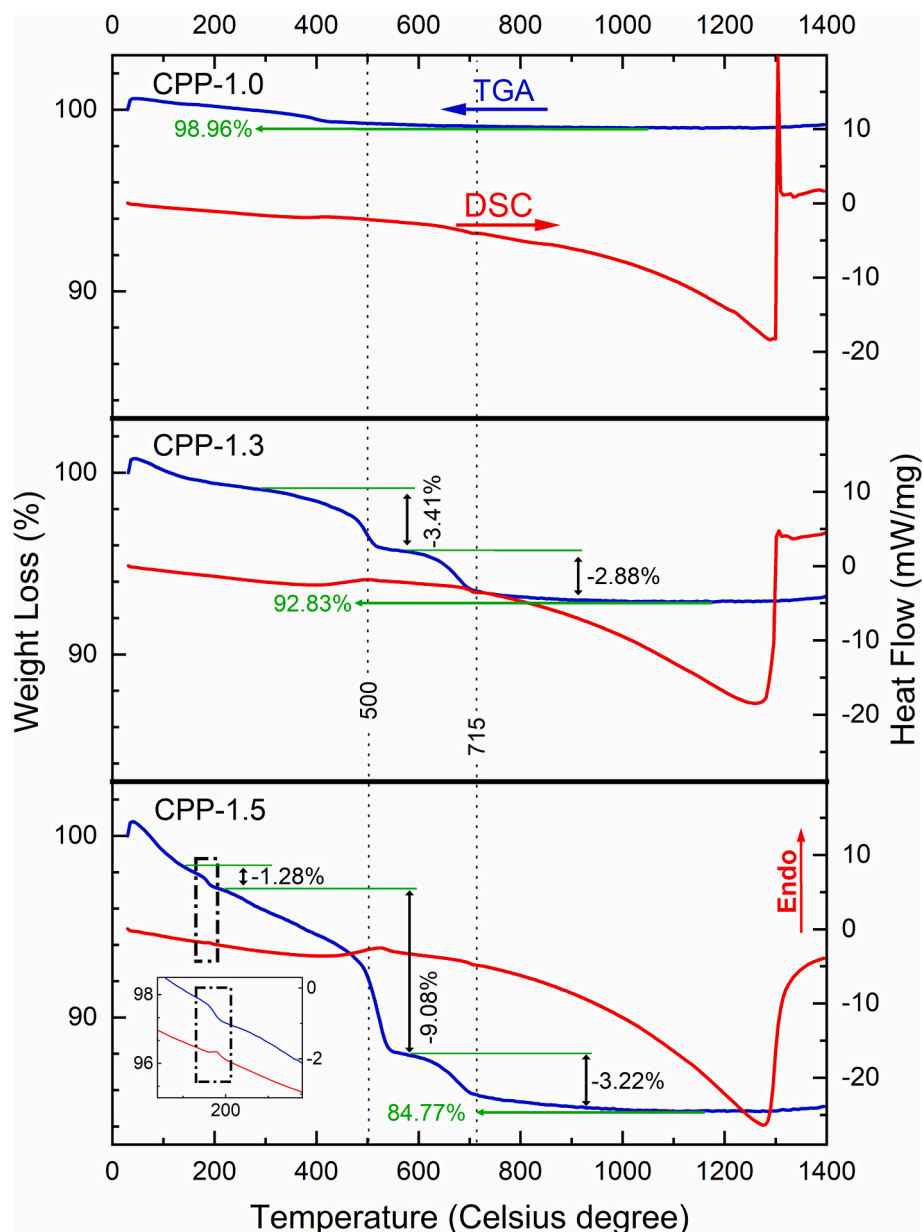


Fig. 2. TGA and DSC curves of the collected powders.

CPP-1.5 was measured as 23.3 and 15.5  $m^2/g$ , respectively, from their BET plot (Fig. 3b). Moreover, CPP-1.0 SSA was calculated as high as 61.9  $m^2/g$ , while researchers using other methods to synthesize  $\beta$ -CPP have reported <29  $m^2/g$  [7,14,15].

Fig. 4 presents SEM and TEM micrographs of the samples with HR-TEM images of their nanoparticles, as well as their electron diffraction patterns. As can be seen in Fig. 4(a-c), the CPP-1.3 and CPP-1.5 particles are mostly aggregated plate-like particles, while for CPP-1, most of the  $\beta$ -CPP particles are spherical. The SEM images support the above-discussed results of the isotherms. Thus, LFS has another advantage over other methods in addition to the high SSA since spherical particles are often favored in many bio-applications [42,43]. To the best of our knowledge,  $\beta$ -CPP forms plate-like particles during synthesis process of other methods, as CPP particles have an anisotropic nature [7–10,17–21]. The CPP particles go through the phase transformation from brushite crystals, which results in plate-like particles, as the reference XRD pattern of brushite has a main peak at low angles which

has high intensity in comparison with other peaks [44]. Therefore, the subsequent phases (such as  $\gamma$ -CPP and then  $\beta$ -CPP) tend to preserve the morphological features and form plate-like particles as well. On the other hand, the fast thermodynamic uniform growth of all crystal facets in the gas phase in the high-temperature flame can directly cause the formation of spherical and/or near-spherical  $\beta$ -CPP particles. In addition,  $\beta$ -CPP synthesized particles have different porous structures with varying pore sizes, as can be seen in Fig. 4(d and g), resulting in the high SSA. Lots of nanosized particles could be synthesized by LFS have been seen on the surface of spherical particles, as has been illustrated in the TEM (Fig. 4j) and high magnification SEM images (Fig. 4(g and e)) for the CPP-1.0 and CPP-1.3. In addition, they can be seen on the surface of the plate-like particles (Fig. 4f). Therefore,  $\beta$ -CPP nanoparticles can be synthesized by the LFS method, and with adjustment of the synthesis parameters, the fraction of nanoparticles could be increased in our future work. Applying different aerosol methods using size segregation might also enable the collection of a specific size range [45].

As Fig. 4(h and k) show, most of the synthesized nanoparticles are approximately 10 nm in diameter with the  $\beta$ -CPP crystalline phase



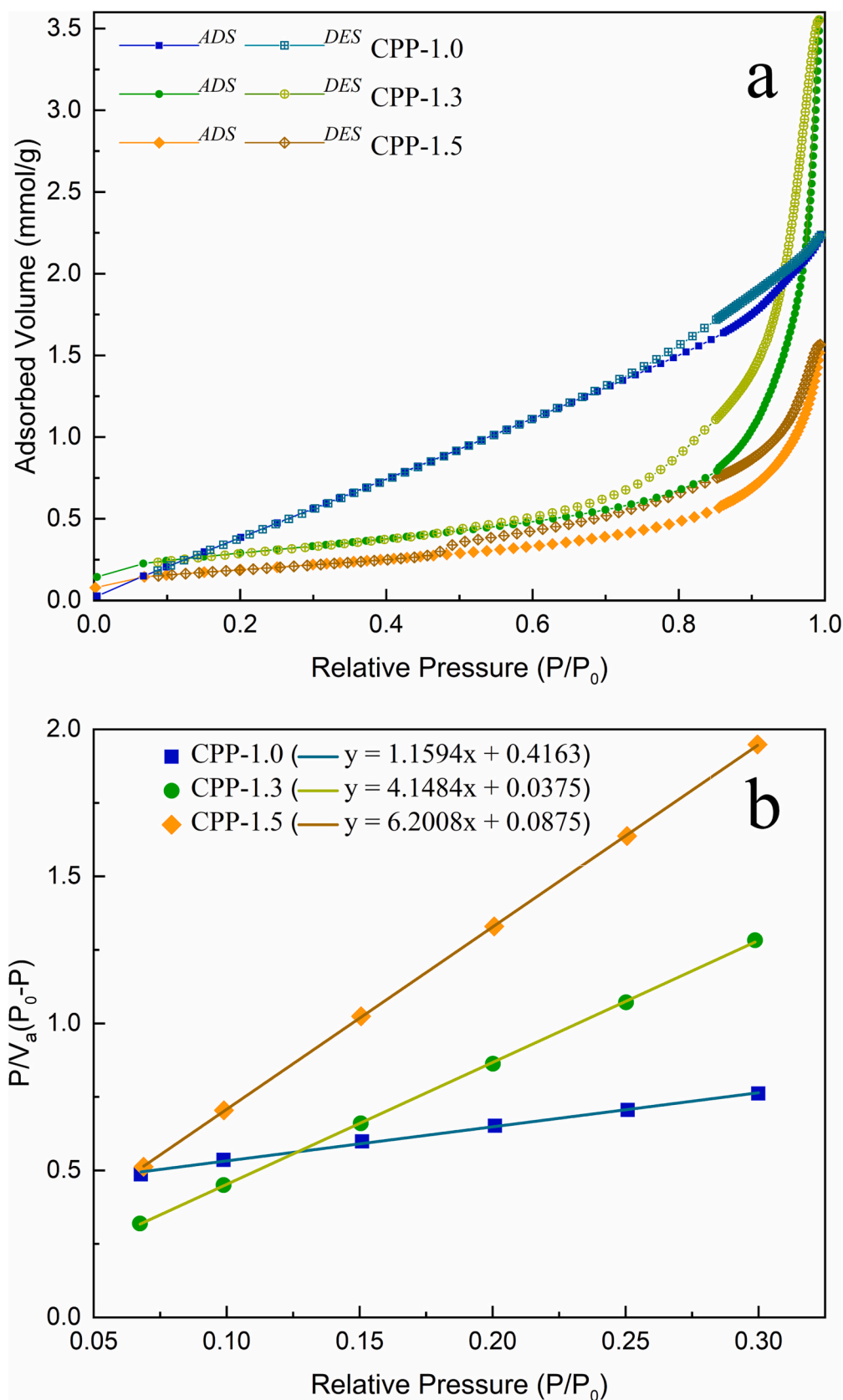


Fig. 3.  $N_2$  adsorption-desorption isotherms (a) and BET plots (b) of the synthesized samples.

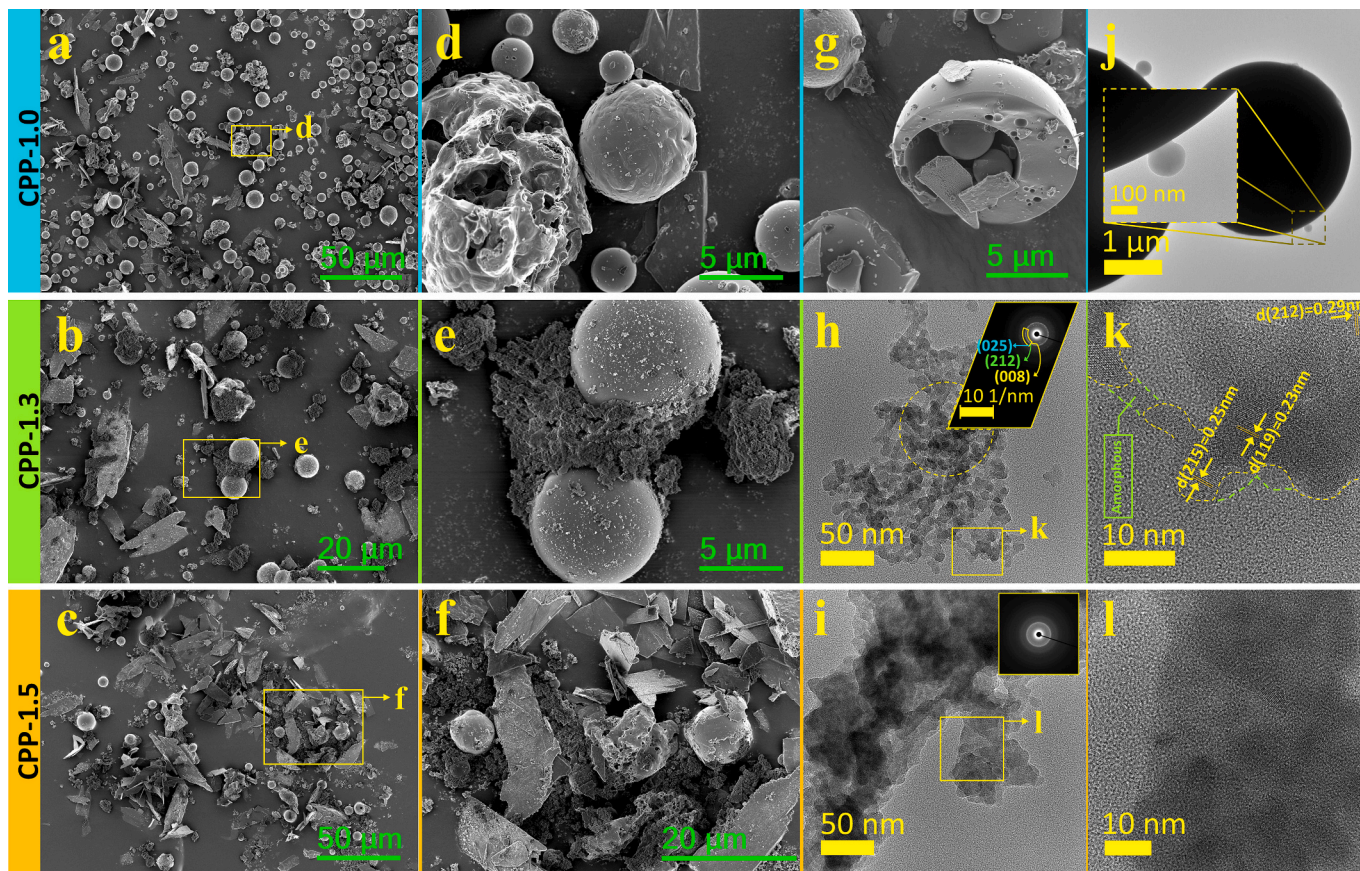


Fig. 4. (a-g) SEM and (h-l) TEM micrographs with the HR-TEM images of the corresponding nanoparticles of the samples.

because their lattice fringe distances, and electron diffraction pattern are in good agreement with the XRD results. In addition, there could be some amorphous nanoparticles in CPP-1.3, as no lattice fringes could be seen for a few nanoparticles. As can be seen in Fig. 4(i) and (l), the

nanoparticles of CPP-1.5 are more strongly aggregated, and there are fewer lattice fringes. That can also be due to presence of different phases, and thus overlapping of their lattice fringes.

Fig. 5 illustrates that synthesized CPP-1.0 and -1.3 micro-and

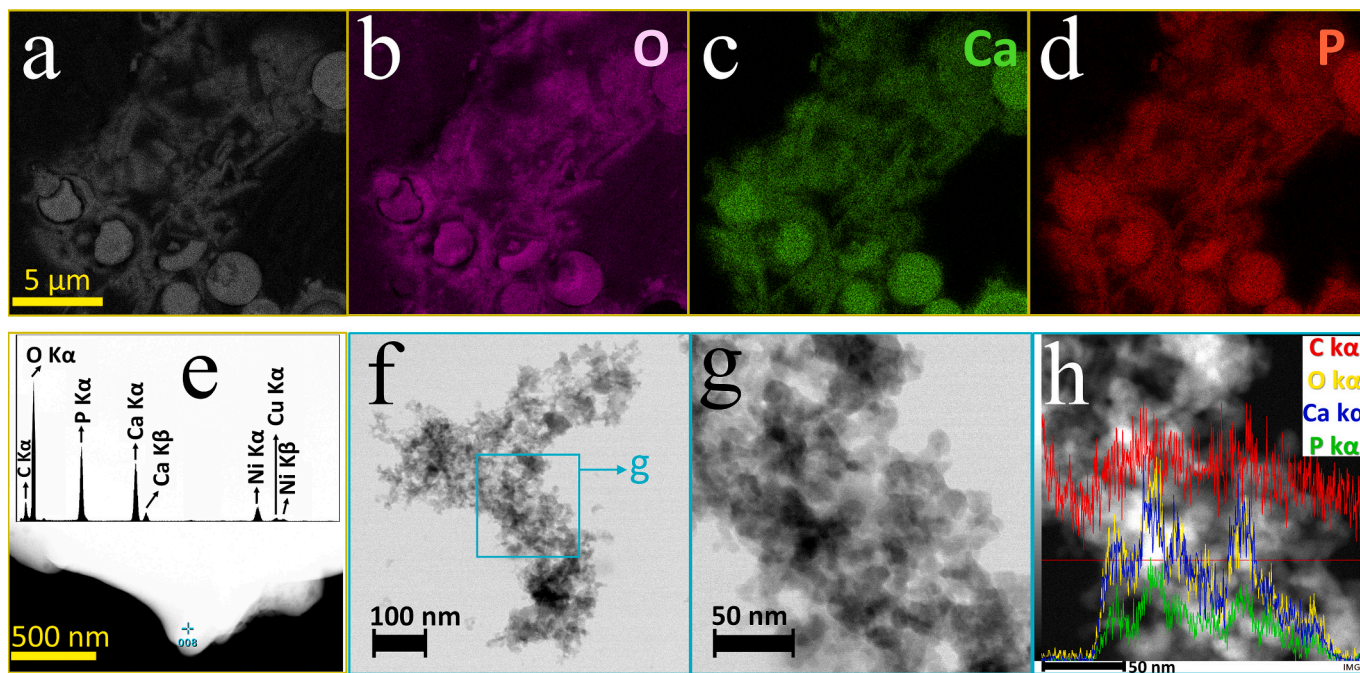


Fig. 5. a-d) SEM-EDX mapping images of the CPP-1.0. e) Dark-field STEM image of a CPP-1.0 nanoparticle, which is located on a bigger particle, with its EDX analysis. f-h) Bright-field STEM micrographs of CPP-1.3 nanoparticles, and their corresponding EDX line-scan.



nanoparticles consist only of evenly distributed Ca, O, and P. Besides, the ratio of Ca/P is almost equal to 1 in the EDX analysis of the CPP-1.0 nanoparticle (Fig. 5e). Moreover, for CPP-1.3 nanoparticles, the P element EDX line profile follows the Ca profile for different nanoparticles in the scanned line (Fig. 5h).

#### 4. Conclusions

All in all, we have shown in this study that it is possible to generate single-phase nanocrystalline  $\beta$ -CPP micro-and nanoparticles by LFS without post-heat treatment. In general, we believe that flame synthesis offers a convenient way to generate applicable CP materials for various applications.

#### Funding

This work was supported by the Doctoral School of Tampere University and Academy of Finland, nSTAR project, [grant number 339545].

#### CRediT authorship contribution statement

**Alireza Charmforoushan:** Writing – original draft, Conceptualization, Methodology, Validation, Formal analysis, Investigation, Visualization. **Miika Sorvali:** Writing – review & editing, Validation, Methodology. **Jyrki M. Mäkelä:** Writing – review & editing, Supervision, Project administration, Funding acquisition.

#### Declaration of competing interest

The authors declare that they have no known competing financial interests or personal relationships that could have appeared to influence the work reported in this paper.

#### Data availability

No data was used for the research described in the article.

#### Acknowledgements

The financial support of the Doctoral School of Tampere University and nSTAR project is highly appreciated. We would like to thank the technical assistance by Dr. Mari Honkanen from Tampere Microscopy Center.

#### References

- [1] L.M. Grover, A.J. Wright, U. Gbureck, A. Bolarinwa, J. Song, Y. Liu, D.F. Farrar, G. Howling, J. Rose, J.E. Barralet, The effect of amorphous pyrophosphate on calcium phosphate cement resorption and bone generation, *Biomaterials*. 34 (2013) 6631–6637, <https://doi.org/10.1016/j.biomaterials.2013.05.001>.
- [2] T.H.A. Correa, R. Toledo, N.S. Silva, J.N.F. Holanda, Novel nano-sized biphasic calcium phosphate bioceramics ( $\beta$ -CPP/ $\beta$ -TCP) derived of lime mud waste, *Mater. Lett.* 243 (2019) 17–20, <https://doi.org/10.1016/j.matlet.2019.02.020>.
- [3] H. Akbari Aghdam, E. Sanatizadeh, M. Motifard, F. Aghadavoudi, S. Saber-Samandari, S. Esmaili, E. Sheikhabahei, M. Safari, A. Khandan, Effect of calcium silicate nanoparticle on surface feature of calcium phosphates hybrid bio-nanocomposite using for bone substitute application, *Powder Technol.* 361 (2020) 917–929, <https://doi.org/10.1016/j.powtec.2019.10.111>.
- [4] A. Charmforoushan, M.R. Roknabadi, N. Shahtahmassebi, B. Malaekhe-Nikouei, M. Bagherabadi, Synthesis and controlled drug release behavior of micro-mesoporous wollastonite nanoparticles. Effect of calcination temperature on the structural and biodegradability properties, *Mater. Chem. Phys.* 280 (2022) 125825, <https://doi.org/10.1016/j.matchemphys.2022.125825>.
- [5] D.C. Bassett, T.E. Robinson, R.J. Hill, L.M. Grover, J.E. Barralet, Self-assembled calcium pyrophosphate nanostructures for targeted molecular delivery, *Biomater. Adv.* 140 (2022) 213086, <https://doi.org/10.1016/j.bioadv.2022.213086>.
- [6] T. Safronova, A. Kiselev, I. Selezneva, T. Shatalova, Y. Lukina, Y. Filippov, O. Tsochev, S. Tikhonova, O. Antonova, A. Knotko, Bioceramics based on  $\beta$ -calcium pyrophosphate, *Materials*. 15 (2022) 3105, <https://doi.org/10.3390/ma15093105>.
- [7] A.D. Anastasiou, M. Nerantzaki, A.P. Brown, A. Jha, D.N. Bikiaris, Drug loading capacity of microporous  $\beta$ -pyrophosphate crystals, *Mater. Des.* 168 (2019) 107661, <https://doi.org/10.1016/j.matdes.2019.107661>.
- [8] A.D. Anastasiou, S. Strafford, O. Posada-Estefan, C.L. Thomson, S.A. Hussain, T. J. Edwards, M. Malinowski, N. Hondow, N.K. Metzger, C.T.A. Brown,  $\beta$ -pyrophosphate: a potential biomaterial for dental applications, *Mater. Sci. Eng. C* 75 (2017) 885–894, <https://doi.org/10.1016/j.msec.2017.02.116>.
- [9] H. Kebiroglu, T. Ates, N. Bulut, I. Ercan, F. Ercan, I.K. Acari, S. Koytepe, B. Ates, O. Kaygili, The effects of Zn/Fe co-dopants on the structural, thermal, magnetic, and in vitro biocompatibility properties of calcium pyrophosphate ceramics, *Phys. B Condens. Matter* 643 (2022) 414123, <https://doi.org/10.1016/j.physb.2022.414123>.
- [10] I. Chrysafi, E. Kontonasi, A.D. Anastasiou, D. Patsiaoura, L. Papadopoulou, G. Vourlias, E. Vouvioudi, D. Bikiaris, Mechanical and thermal properties of PMMA resin composites for interim fixed prostheses reinforced with calcium  $\beta$ -pyrophosphate, *J. Mech. Behav. Biomed. Mater.* 112 (2020) 104094, <https://doi.org/10.1016/j.jmbbm.2020.104094>.
- [11] Y.Y. Li, D.A. Yang, H. Zhao, Degradation behavior of  $\beta$ -Ca<sub>3</sub>(PO<sub>4</sub>)<sub>2</sub>/ $\beta$ -Ca<sub>2</sub>P<sub>2</sub>O<sub>7</sub> bioceramics, in: *Key Eng. Mater., Trans Tech Publ*, 2007, pp. 1650–1653, <https://doi.org/10.4028/www.scientific.net/KEM.336-338.1650>.
- [12] X.L. Wang, H.S. Fan, X.D. Zhang, An improvement in sintering property of  $\beta$ -tricalcium phosphate by addition of calcium pyrophosphate and calcium carbonate, *Mater. Sci. Forum, Trans. Tech. Publ.* (2005) 2359–2362, <https://doi.org/10.4028/www.scientific.net/MSF.475-479.2359>.
- [13] K.-S. Lee, H.-S. Han, Y.-C. Kim, J.H. Lo Han, H. Seung, H.-S. Lee, J.-S. Chang, D.-H. Lee, Evaluation of porous  $\beta$ -calcium pyrophosphate as bioresorbable bone graft substitute material, *Mater. Res. Innov.* 19 (2015) 86–90, <https://doi.org/10.1179/1433075X14Y.00000000215>.
- [14] D. Griesiute, J. Gaidukevic, A. Zarkov, A. Kareiva, Synthesis of  $\beta$ -Ca<sub>2</sub>P<sub>2</sub>O<sub>7</sub> as an adsorbent for the removal of heavy metals from water, *Sustainability*. 13 (2021) 7859, <https://doi.org/10.3390/su13147859>.
- [15] V.C. Ghantani, M.K. Dongare, S.B. Umbarkar, Nonstoichiometric calcium pyrophosphate: a highly efficient and selective catalyst for dehydration of lactic acid to acrylic acid, *RSC Adv.* 4 (2014) 33319–33326, <https://doi.org/10.1039/C4RA06429A>.
- [16] R. Baitahe, C. Sronsri, S. Thompho, K. Chaiseeda, N. Montri, B. Boonchom, Correlation between structure, chromaticity, and dielectric properties of calcium copper pyrophosphates, Ca<sub>2</sub>–x Cu<sub>x</sub> P<sub>2</sub>O<sub>7</sub>, *Sci. Rep.* 12 (2022) 6869, <https://doi.org/10.1038/s41598-022-11056-4>.
- [17] G. Apsana, P.P. George, N. Devanna, Facile green synthesis and characterization of calcium pyrophosphate nanoparticles using D-Glucose, *Mater. Today Proc.* 4 (2017) 10913–10920, <https://doi.org/10.1016/j.matpr.2017.08.046>.
- [18] D. Griesiute, E. Garskaite, A. Antuzevics, V. Klimavicius, V. Balevicius, A. Zarkov, A. Katelnikovas, D. Sandberg, A. Kareiva, Synthesis, structural and luminescent properties of Mn-doped calcium pyrophosphate (Ca<sub>2</sub>P<sub>2</sub>O<sub>7</sub>) polymorphs, *Sci. Rep.* 12 (2022) 7116, <https://doi.org/10.1038/s41598-022-11337-y>.
- [19] J. Roman-Lopez, I.B. Lozano, E. Cruz-Zaragoza, J.I.G. Castañeda, J.A.I. Díaz-Góngora, Synthesis of  $\beta$ -Ca<sub>2</sub>P<sub>2</sub>O<sub>7</sub>:Tb<sup>3+</sup> to gamma radiation detection by thermoluminescence, *Appl. Radiat. Isot.* 124 (2017) 44–48, <https://doi.org/10.1016/j.apradiso.2017.03.004>.
- [20] I.B. Lozano, J. Roman-Lopez, R. Sosa, J.A.I. Díaz-Góngora, J. Azorín, Preparation of cerium doped calcium pyrophosphate: study of luminescent behavior, *JOL* 173 (2016) 5–10, <https://doi.org/10.1016/j.jlumin.2015.12.032>.
- [21] G. Fan, C. Lin, W. Yang, Y. Guan, Y. Liu, L. Wang, Concentration induced site symmetry transformation of Eu<sup>3+</sup> luminescence center in  $\beta$ -Ca<sub>2</sub>P<sub>2</sub>O<sub>7</sub>, *Mater. Res. Bull.* 80 (2016) 64–71, <https://doi.org/10.1016/j.materresbull.2016.03.016>.
- [22] K.K. Gupta, S. Dhoble, A.R. Krupski, Facile synthesis and thermoluminescence properties of nano bio-ceramic  $\beta$ -Ca<sub>2</sub>P<sub>2</sub>O<sub>7</sub>: Dy phosphor irradiated with 75 meV C<sub>6+</sub> ion beam, *Sci. Rep.* 10 (2020) 21203, <https://doi.org/10.1038/s41598-020-78365-4>.
- [23] T.H.A. Corrêa, J.N.F. Holanda, Calcium pyrophosphate powder derived from avian eggshell waste, *Cerâmica*. 62 (2016) 278–280, <https://doi.org/10.1590/0366-69132016623631986>.
- [24] Z. Zyman, A. Goncharenko, O. Khavroniuk, D. Rokhmistrov, Crystallization of metastable and stable phases from hydrolyzed by rinsing precipitated amorphous calcium phosphates with a given Ca/P ratio of 1:1, *J. Cryst. Growth* 535 (2020) 125547, <https://doi.org/10.1016/j.jcrysgro.2020.125547>.
- [25] A. Charmforoushan, M.R. Roknabadi, N. Shahtahmassebi, B. Malaekhe-Nikouei, Low temperature facile synthesis of pseudowollastonite nanoparticles by the surfactant-assisted sol-gel method, *Mater. Chem. Phys.* 243 (2020) 122629, <https://doi.org/10.1016/j.matchemphys.2020.122629>.
- [26] Q. Zuo, W. Liu, Y. Su, Y. Cao, K. Ren, Y. Wang, Synthesis of LiCoO<sub>2</sub> cathode materials for Li-ion batteries at low temperatures, *Scr. Mater.* 233 (2023) 115511, <https://doi.org/10.1016/j.scriptamat.2023.115511>.
- [27] K. Li, H. Li, S. Huang, X. Luo, H. Jin, Ultra-low temperature solid-state synthesis of single-phase SrY<sub>2</sub>O<sub>4</sub> for thermal-barrier-coating applications, *Powder Technol.* 423 (2023) 118494, <https://doi.org/10.1016/j.powtec.2023.118494>.
- [28] R. Mueller, R. Jossen, S.E. Pratsinis, M. Watson, M.K. Akhtar, Zirconia nanoparticles made in spray flames at high production rates, *J. Am. Ceram. Soc.* 87 (2004) 197–202, <https://doi.org/10.1111/j.1551-2916.2004.00197.x>.
- [29] A.J. Gröhn, S.E. Pratsinis, A. Sánchez-Ferrer, R. Mezzenga, K. Wegner, Scale-up of nanoparticle synthesis by flame spray pyrolysis: the high-temperature particle residence time, *Ind. Eng. Chem. Res.* 53 (2014) 10734–10742, <https://doi.org/10.1021/ie501709s>.

- [30] M. Aromaa, H. Keskinen, J.M. Mäkelä, The effect of process parameters on the Liquid Flame Spray generated titania nanoparticles, *Proc. Symp. J Surf. Funct. Biomater.* 24 (2007) 543–548, <https://doi.org/10.1016/j.bioeng.2007.08.004>.
- [31] K.J. Brobbey, J. Haapanen, M. Tuominen, J. Mäkelä, M. Gunell, E. Eerola, J. J. Saarinen, M. Toivakka, High-speed production of antibacterial fabrics using liquid flame spray, *Text. Res. J.* 90 (2020) 503–511, <https://doi.org/10.1177/0040517519866952>.
- [32] J.M. Mäkelä, J. Haapanen, J. Harra, P. Juuti, S. Kujanpää, Liquid flame spray—a hydrogen-oxygen flame based method for nanoparticle synthesis and functional nanocoatings, *Kona Powder Part. J.* 34 (2017) 141–154, <https://doi.org/10.14356/kona.2017020>.
- [33] M. Sorvali, M. Honkanen, L. Hyvärinen, R. Kuisma, J. Larjo, J.M. Mäkelä, Crystallographic phase formation of iron oxide particles produced from iron nitrate by liquid flame spray with a dual oxygen flow, *Int. J. Ceram. Eng. Sci.* 3 (2021) 227–236.
- [34] M. Sorvali, M. Nikka, P. Juuti, M. Honkanen, T. Salminen, L. Hyvärinen, J. M. Mäkelä, Controlling the phase of iron oxide nanoparticles fabricated from iron (III) nitrate by liquid flame spray, *Int. J. Ceram. Eng. Sci.* 1 (2019) 194–205, <https://doi.org/10.1002/ces2.10025>.
- [35] I. Jönkkäri, M. Sorvali, H. Huhtinen, E. Sarlin, T. Salminen, J. Haapanen, J. M. Mäkelä, J. Vuorinen, Characterization of bidisperse magnetorheological fluids utilizing maghemite ( $\gamma$ -Fe<sub>2</sub>O<sub>3</sub>) nanoparticles synthesized by flame spray pyrolysis, *Smart Mater. Struct.* 26 (2017) 095004.
- [36] T.R. Machado, J.S. da Silva, R.R. Miranda, V. Zucolotto, M.S. Li, M. Valle Martínez de Yuso, J.J. Guerrero-González, I.L.V. Rosa, M. Algarra, E. Longo, Amorphous calcium phosphate nanoparticles allow fingerprint detection via self-activated luminescence, *Chem. Eng. J.* 443 (2022) 136443, <https://doi.org/10.1016/j.cej.2022.136443>.
- [37] M. Edén, Structure and formation of amorphous calcium phosphate and its role as surface layer of nanocrystalline apatite: implications for bone mineralization, *Materialia*. 17 (2021) 101107, <https://doi.org/10.1016/j.mtla.2021.101107>.
- [38] M. Basak, M.L. Rahman, M.F. Ahmed, B. Biswas, N. Sharmin, The use of X-ray diffraction peak profile analysis to determine the structural parameters of cobalt ferrite nanoparticles using Debye-Scherrer, Williamson-hall, Halder-Wagner and size-strain plot: different precipitating agent approach, *J. Alloys Compd.* 895 (2022) 162694, <https://doi.org/10.1016/j.jallcom.2021.162694>.
- [39] M. Rabei, A. Palevicius, A. Monshi, S. Nasiri, A. Vilkauskas, G. Janusas, Comparing methods for calculating nano crystal size of natural hydroxyapatite using X-ray diffraction, *Nanomaterials*. 10 (2020) 1627, <https://doi.org/10.3390/nano10091627>.
- [40] M. Maciejewski, T.J. Brunner, S.F. Loher, W.J. Stark, A. Baiker, Phase transitions in amorphous calcium phosphates with different ca/P ratios, *Thermochim. Acta* 468 (2008) 75–80, <https://doi.org/10.1016/j.tca.2007.11.022>.
- [41] K.S. Sing, Reporting physisorption data for gas/solid systems with special reference to the determination of surface area and porosity (Recommendations 1984), *Pure Appl. Chem.* 57 (1985) 603–619, <https://doi.org/10.1351/pac198557040603>.
- [42] X. Huang, X. Teng, D. Chen, F. Tang, J. He, The effect of the shape of mesoporous silica nanoparticles on cellular uptake and cell function, *Biomaterials*. 31 (2010) 438–448, <https://doi.org/10.1016/j.biomaterials.2009.09.060>.
- [43] D.J. Misiek, J.N. Kent, R.F. Carr, Soft tissue responses to hydroxylapatite particles of different shapes, *J. Oral Maxillofac. Surg.* 42 (1984) 150–160, [https://doi.org/10.1016/S0278-2391\(84\)80025-7](https://doi.org/10.1016/S0278-2391(84)80025-7).
- [44] E. Boanini, F. Silingardi, M. Gazzano, A. Bigi, Synthesis and hydrolysis of brushite (DCPD): the role of ionic substitution, *Cryst. Growth Des.* 21 (2021) 1689–1697, <https://doi.org/10.1021/acs.cgd.0c01569>.
- [45] W.C. Hinds, Y. Zhu, *Aerosol Technology: Properties, Behavior, and Measurement of Airborne Particles*, John Wiley & Sons, 2022.